
E-SQUID

List of Parties

Grant Agreement number: 262947

Project acronym: E-SQUID

Project title: Development of SQUID-based multiplexers for large Infrared-to-X-ray imaging detector arrays in astronomical research from space

HELSINGIN YLIOPISTO, the Coordinator,
Name: Juhani Huovelin
Position: Research Coordinator
Tel.: +358 2941 22948
Fax: + 358 2941 48802
E-mail: juhani.huovelin@helsinki.fi
Address: P.O.Box 48
FI-00014 University of Helsinki,
Finland

Street address:
Department of Physics
Erik Palmenin aukio 1
FI-00560 Helsinki
Finland

UNIVERSITY OF LEICESTER,
Name: Dr. Paul Drumm
Position: Director
Tel.: +44 116 2297707
Fax: +44 116 252 2464
E-mail: pd128@leicester.ac.uk
Address: Space Research Centre
Dept of Physics and Astronomy
Michael Atiyah Building
University of Leicester
University Road
Leicester LE1 7RH
United Kingdom

STICHTING SRON NETHERLANDS INSTITUTE FOR SPACE RESEARCH,
Name: Jan van der Kuur
Position: Instrument Scientist
Tel.: +31 887775862
Fax: +
E-mail: j.van.der.kuur@sron.nl
Address: Sorbonnelaan 2
3584 CA Utrecht
the Netherlands

MAX PLANCK GESELLSCHAFT ZUR FOERDERUNG DER WISSENSCHAFTEN E.V.,
Name: Dr. Ernst Kreysa
Position:
Tel.: +49-(0)228-525269
Fax: +49-(0)228-525229
E-mail: ekreysa@mpifr-bonn.mpg.de
Address: Auf dem Huegel 69, 53121 Bonn, Germany

VALTION TEKNILLINEN TUTKIMUSKESKUS,
Name: Mikko Kiviranta
Position: Senior Research Scientist
Tel.: +358 20 722 6453
Fax: +358 20 722 7012
E-mail: Mikko.Kiviranta@vtt.fi
Address: Tietotie 3, 02150 Espoo, Finland

INSTITUT FUER PHOTONISCHE TECHNOLOGIEN E.V.,
Name: Torsten May
Position: Head of Working Group “Quantum Radiometry”
Tel.: +49 3641 206 123
Fax: +49 3641 209 199
E-mail: torsten.may @ ipht-jena.de
Address: Albert-Einstein-Str. 9, D 077543 Jena, Germany

AIVON OY,
Name: Jari Penttilä
Position: CEO
Tel.: +358 400 265501
Fax: +
E-mail: jari@aivon.fi
Address: Tietotie 3, 02150 Espoo, Finland

SUPRACON AG,
Name: Matthias Meyer
Position: CEO
Tel.: +49 3641 675 383
Fax: +49 3641 675 387
E-mail: meyer@supracon.com
Address: Wildenbruchstr. 15, D-07745 Jena, Germany

E-SQUID Final report – Figures

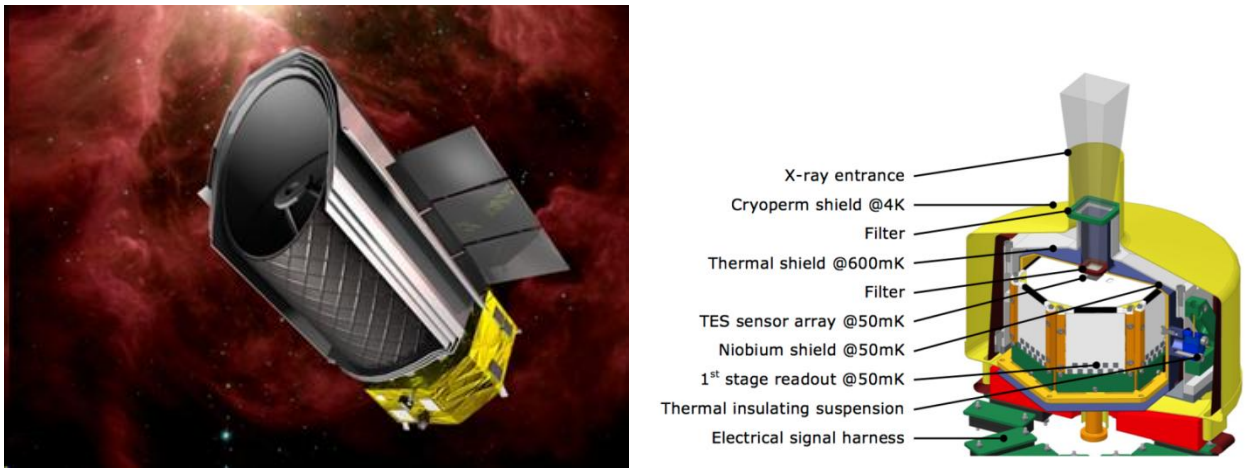

Figure 1. Left: Artists impression of the SPICA spacecraft. Right: 160-pixel detector demonstrator for SAFARI, compatible with FDM readout SQUIDs fabricated in E-SQUID project (© SRON).

Figure 2. Left: Artists impression of the ATHENA+ spacecraft. Right: Current plan for the X-ray Integral Field Unit (X-IFU) instrument (© SRON).

Figure 3. Atacama Large Millimeter/submillimeter Array (ALMA) at Chajnantor plateau in Chile

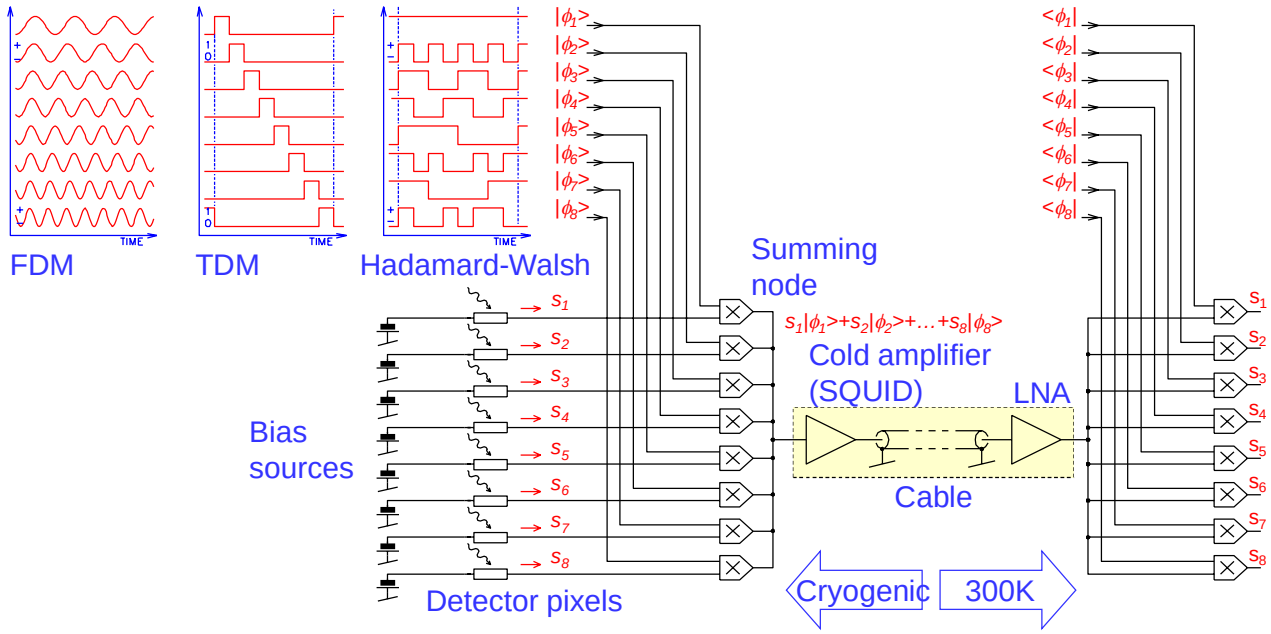

Figure 4. Multiplexing seen as multiplication of signals by orthogonal basis functions. Three basis function sets are depicted: sinusoids (FDM), boxcar functions (Time Domain Multiplexing) and Hadamard codes (Code Domain Multiplexing).

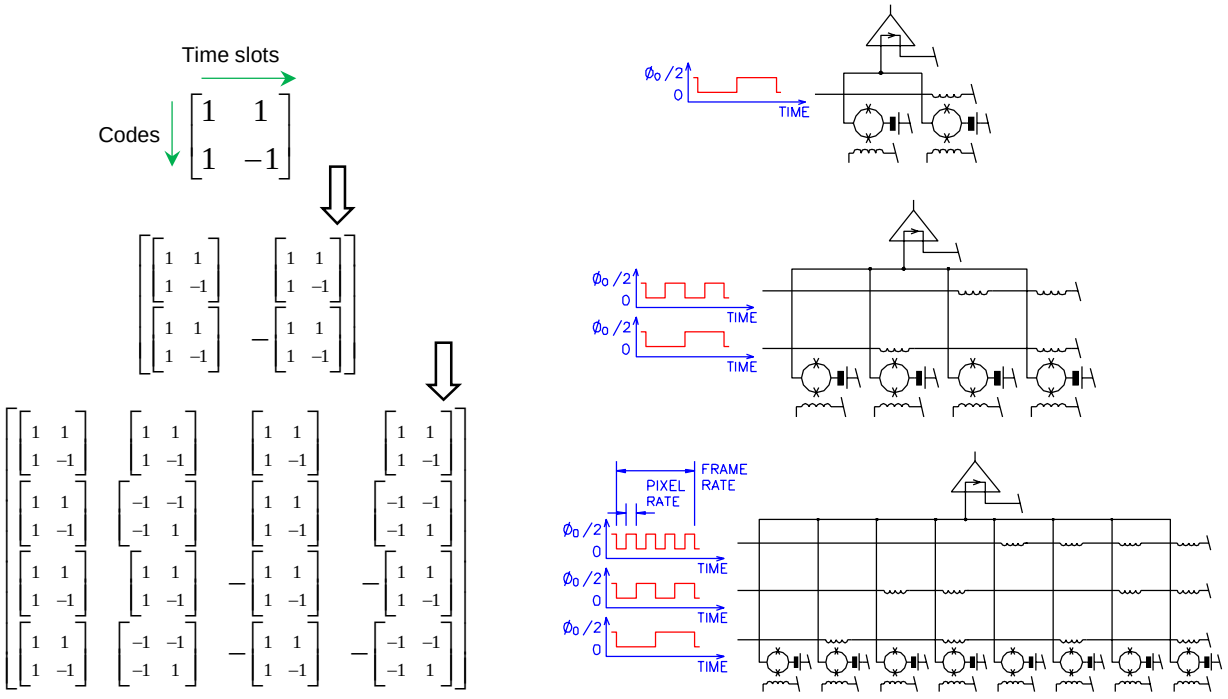

Figure 5. Left: Sylvester's recursive construction of arbitrary large Hadamard matrices. Right: the recursive construction of Hadamard codes implemented in hardware. The technique takes advantage of the periodicity of quantum interference.

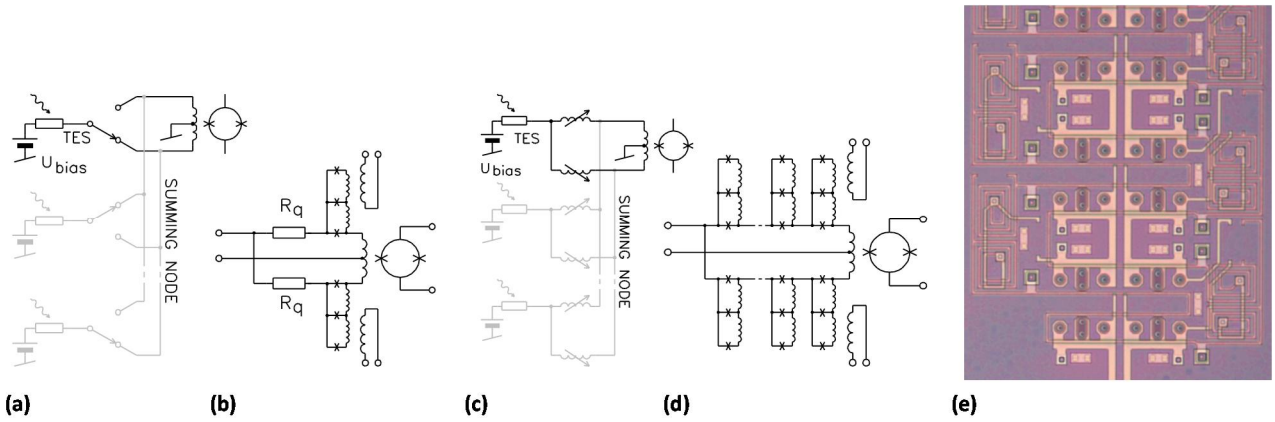

Figure 6. (a) Current steering switches guide the detector current through the SQUID input coil with alternating polarities. (b) Switch realization from flux-controlled Zappe interferometers, version where the blocking-branch interferometer is driven to the resistive finite-voltage state. A resistor R_q in the conductive branch is needed to reach the finite-voltage state. (c) Current steering by inductive dividers. (d) Obtaining large-enough inductance requires a series array of Zappe interferometers. (e) Microphotograph of a realized resistive Zappe array (third metallization is still missing).

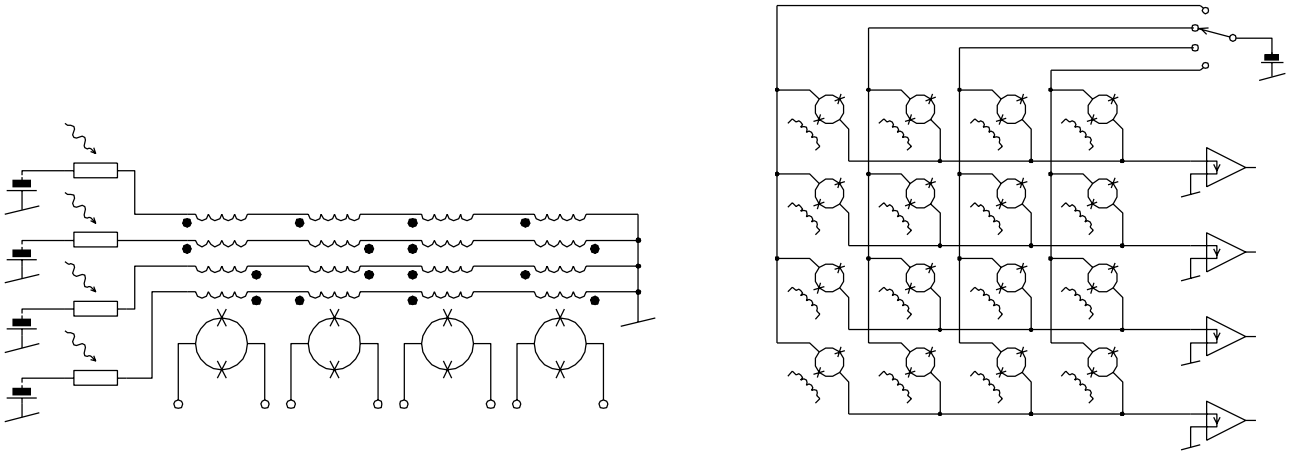

Figure 7. (Left) flux-summing CDM performs the polarity switching by Hadamard-coded SQUID input coils. One SQUID is connected to output at a time, similarly to the TDM. (Right) The only uncomplicated way to reduce the number of cables is to arrange SQUIDs into square. This allows readout of N channels with √N readout lines and √N bias lines.

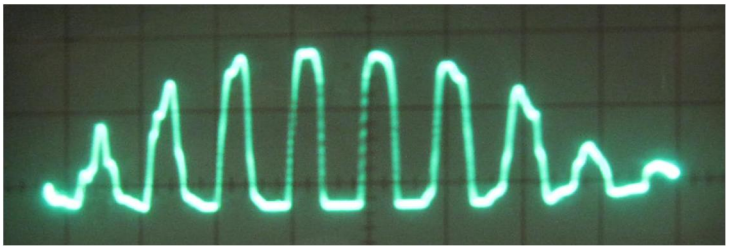

Figure 8. Very strong observed Fraunhofer envelope on the periodic flux response of a 48-series Zappe array spoils its use for the Sylvester-style binary addressing.

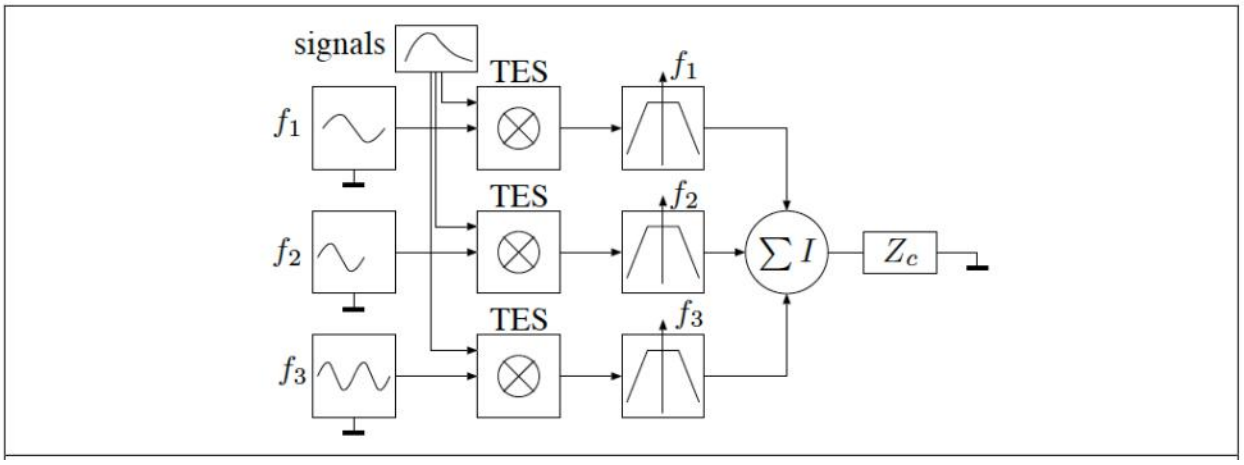

Figure 9: Schematic FDM implementation scheme for a single column. Each TES in a column is biased with a sinusoidal voltage bias of a different frequency. The TESs amplitude modulate the resulting bias currents. The signals are separated in frequency space by means of tuned LC band pass filters, consisting of a coil (L) and capacitor (C). The filtered signals are summed in a current summing point, with finite impedance Z_c, which schematically represents the input impedance of the SQUID current amplifier. The SQUID amplifier chain is not indicated for simplicity.

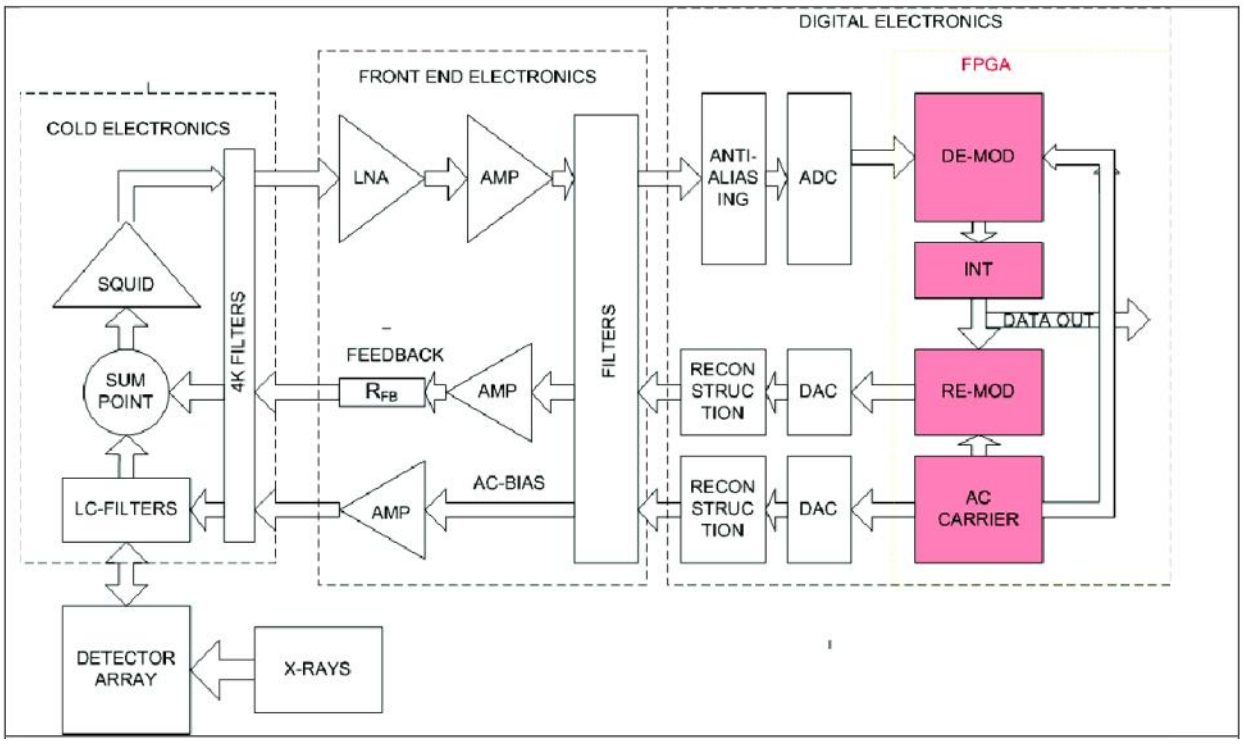

Figure 10: Building blocks of the practical implementation of FDM for TES-based detector readout.

Figure 11: APEX on the Chajnantor plateau at 5100m altitude. The door, seen opened under the dish, is the entrance to the Cassegrain cabin. Only there, a large field of view is available, but not in the cabins around the Nasmyth foci, which are visible on each side.

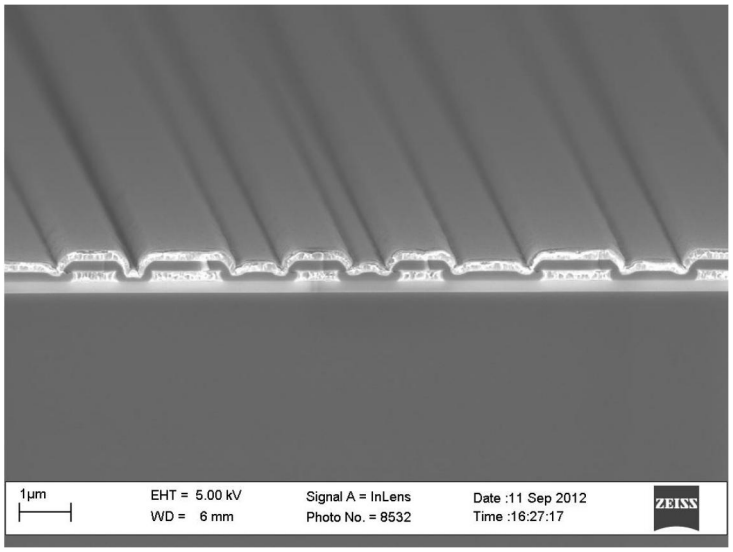

Figure 12: SEM photographed cross-section of a Nb-SiO2-Nb test structure, fabricated using the new selectively deposited insulator

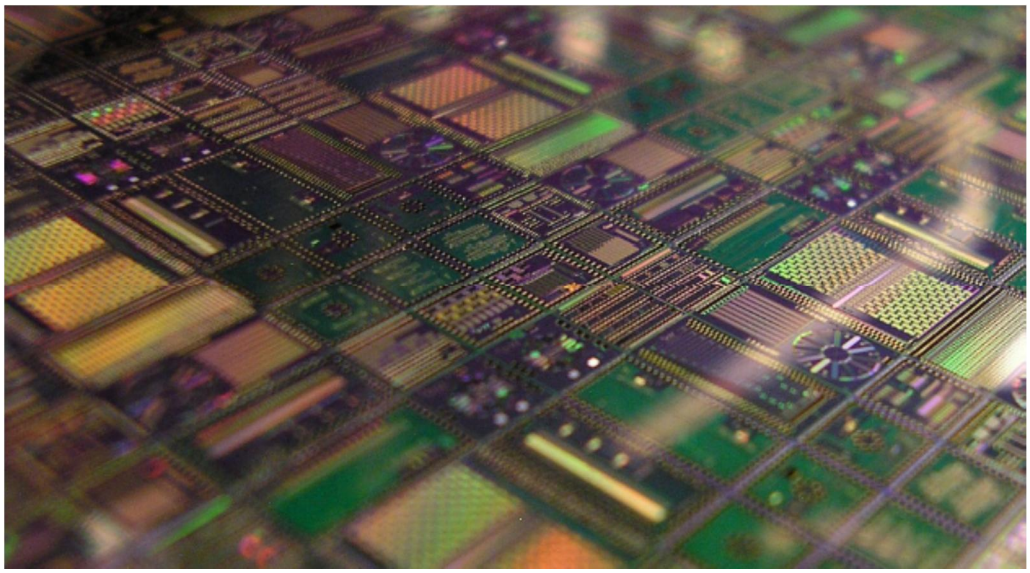

Figure 13: Two adjacent reticle fields in a finished wafer of build 3

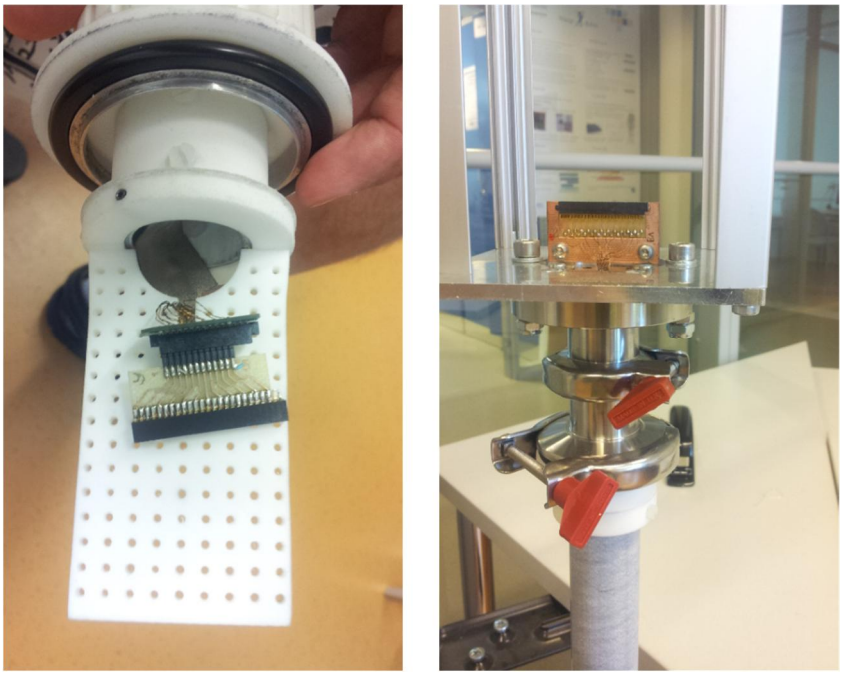

Figure 14. (Left) cold end and (right) warm end of the 'broomstick' liquid helium probe equipped with a modular electronics cage.

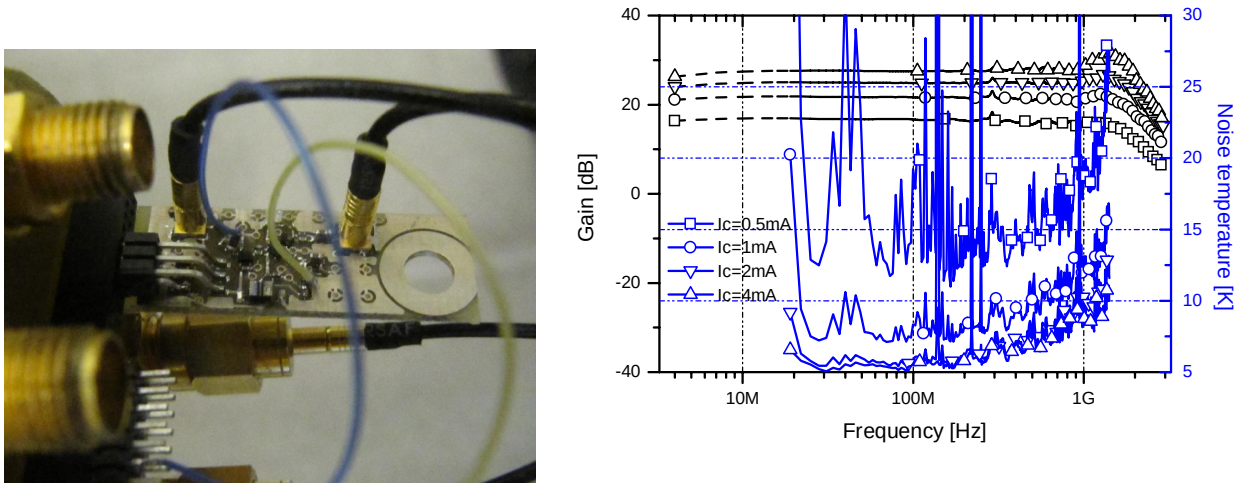

Figure 15. Left: a cryogenic semiconductor LNA attached in a dipstick for testing in liguid helium. Right: measured frequency response and noise temperature of the amplifier at various bias currents.

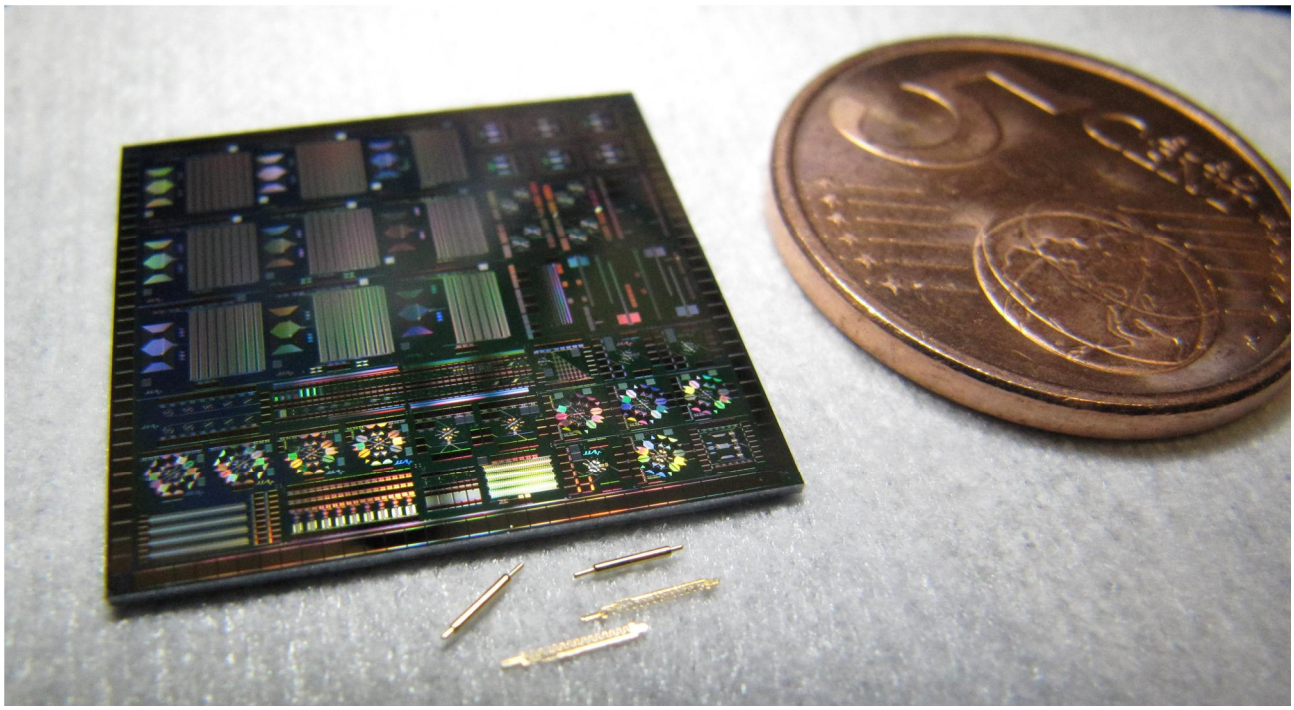

Figure 16. The 20 x 20 mm sized Build 4 reticle is equipped with lithographically routed test wiring, which leads from SQUID chips to the large pads at the outer edge of the reticle. The wiring will get destroyed when the reticle is further diced into chips. A few tentative types of spring loaded contacts are shown in front of the chip, which may make possible electrical contacts to the large test pads, without having to resort to wire bonding.

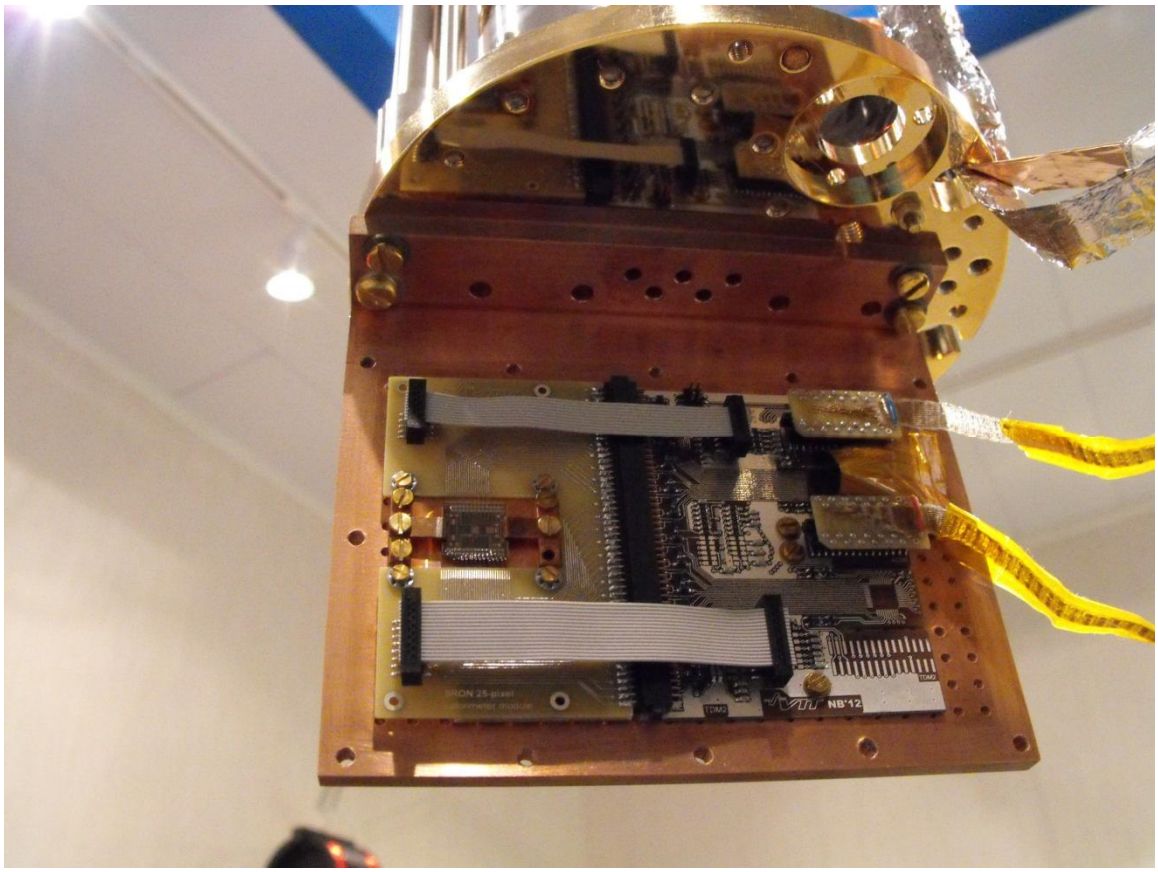

Figure 17. The E-SQUID characterisation equipment installed in UH Cryostat.

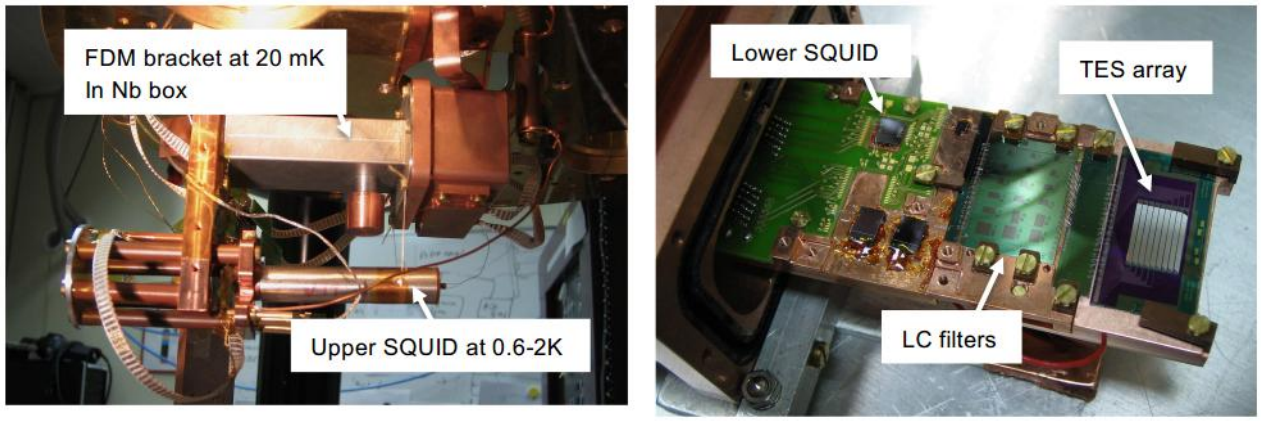

Figure 18: Photograph of the experimental setup in the cryostat in the 2-stage 2-temperature configuration (left), and of the bracket with the FDM multiplexer and TES array (right). On the bracket from right to left one finds the TES chip, an interconnection chip, a LC filter chip, and the 1st and 2nd SQUID stage. The chips are interconnected with superconducting aluminum wire bonds. A Helmholtz coil for magnetic field biasing has been removed for the picture. The bracket is shielded against external magnetic fields and stray light with a niobium box.

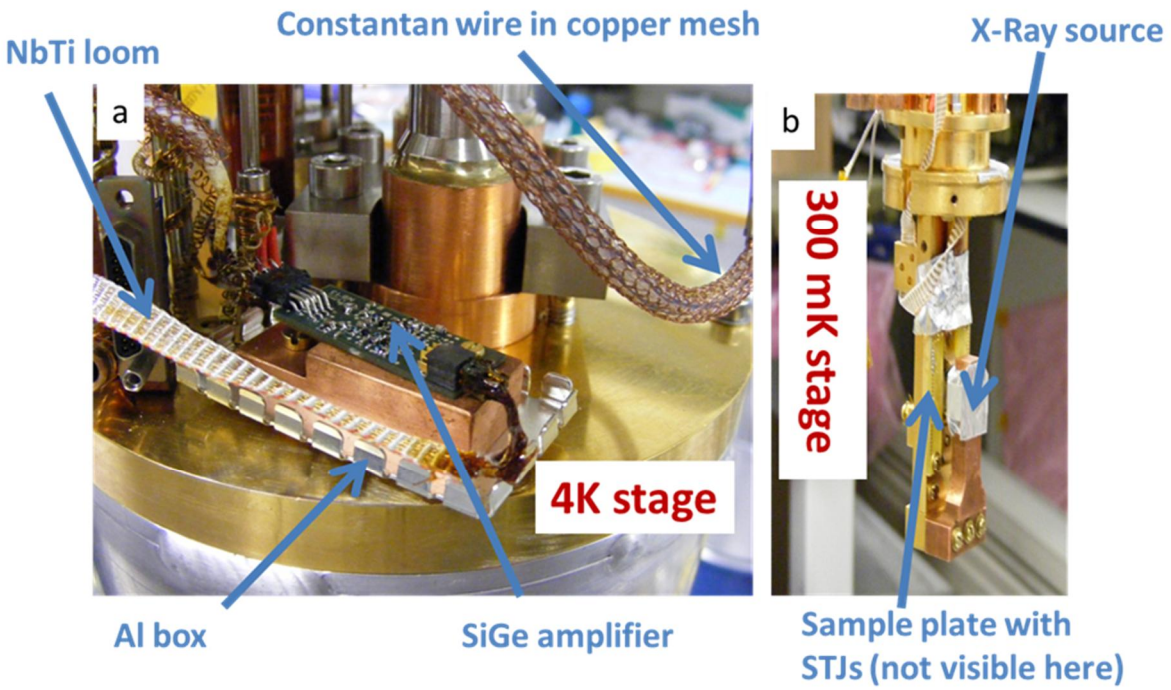

Figure 19: Pictures of the 4K and 300 mK stages

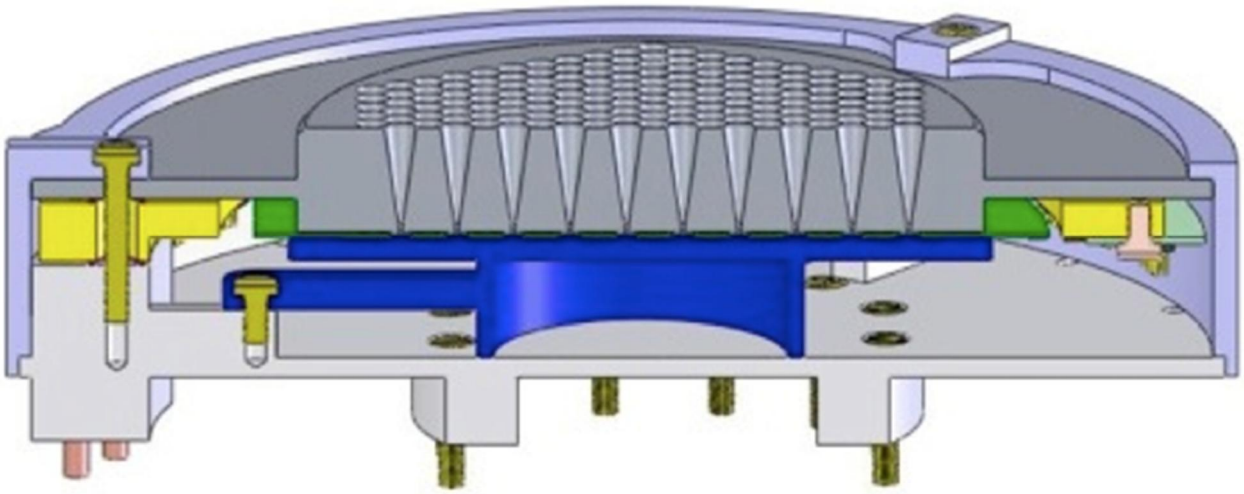

Figure 20: Mechanical scheme of LABOCA-2. The wafer is shown in green, the back short in cyan and the mounting ring in yellow.

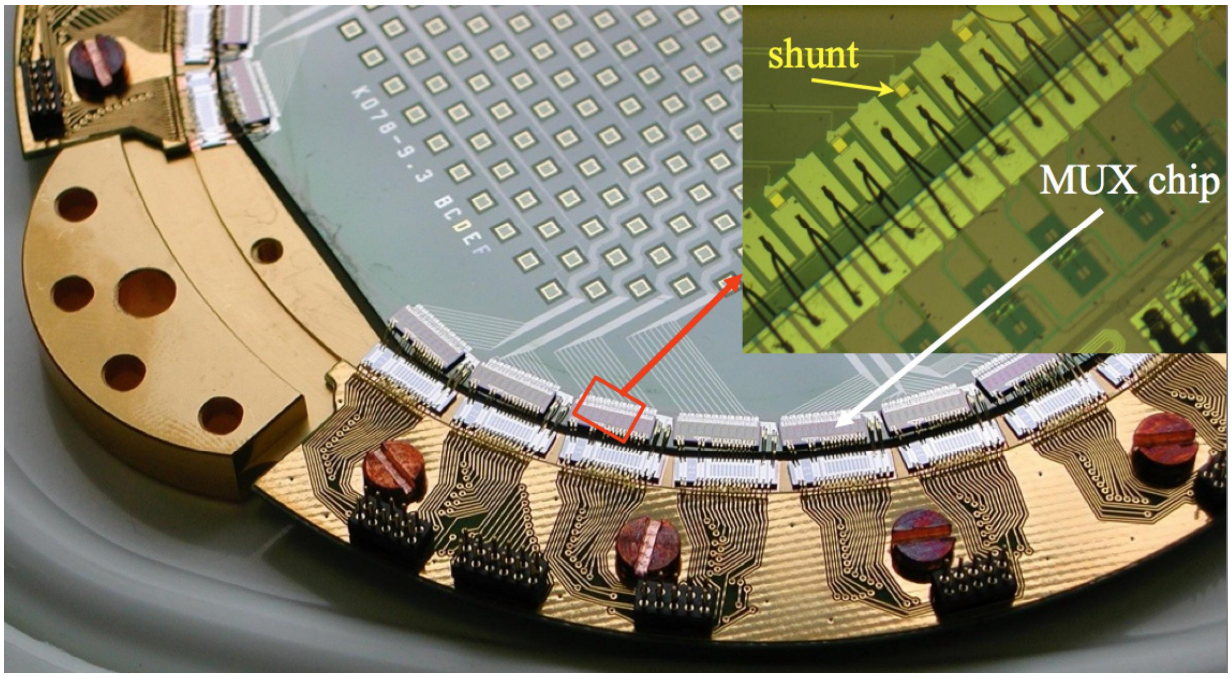

Figure 21: An early version of an LABOCA-2 wafer in its mounting ring

The bias circuit with the shunt resistors is integrated on the wafer. The MUX chips are connected electrically with Al-wire bonds to the wafer and the mounting ring. Thermal contact and mechanical stability is provided by a large number of Au-band bonds from the wafer to the mounting ring

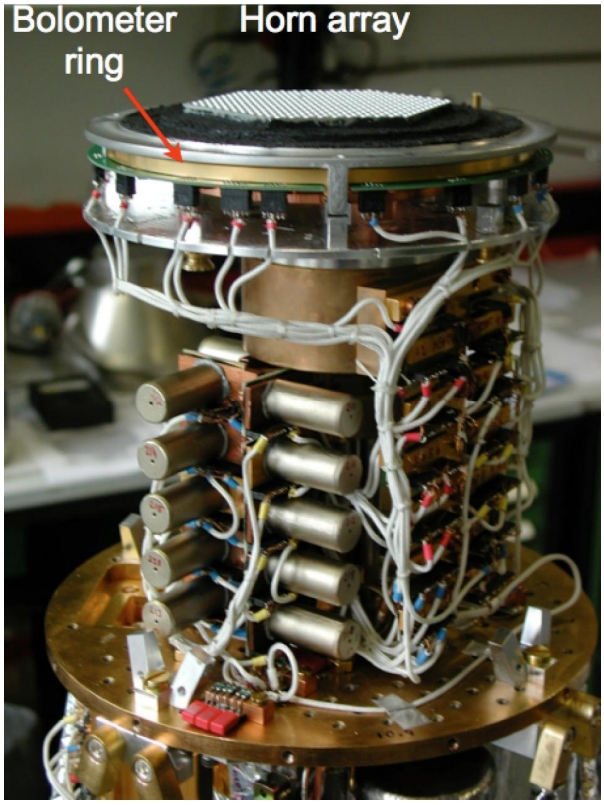

Figure 22: Cold part of the LABOCA-2 cryostat

At the bottom of the figure is the copper cold plate of the pulse tube at 2.4K. Above that, 10 of the 15 Cryoperm beakers, each shielding 2 SQIFs, are visible (800mK). On top are the mounting ring with the TES-wafer and the horn array. In operation, an additional aluminum ring around the the mounting ring provides a complete superconducting shield.

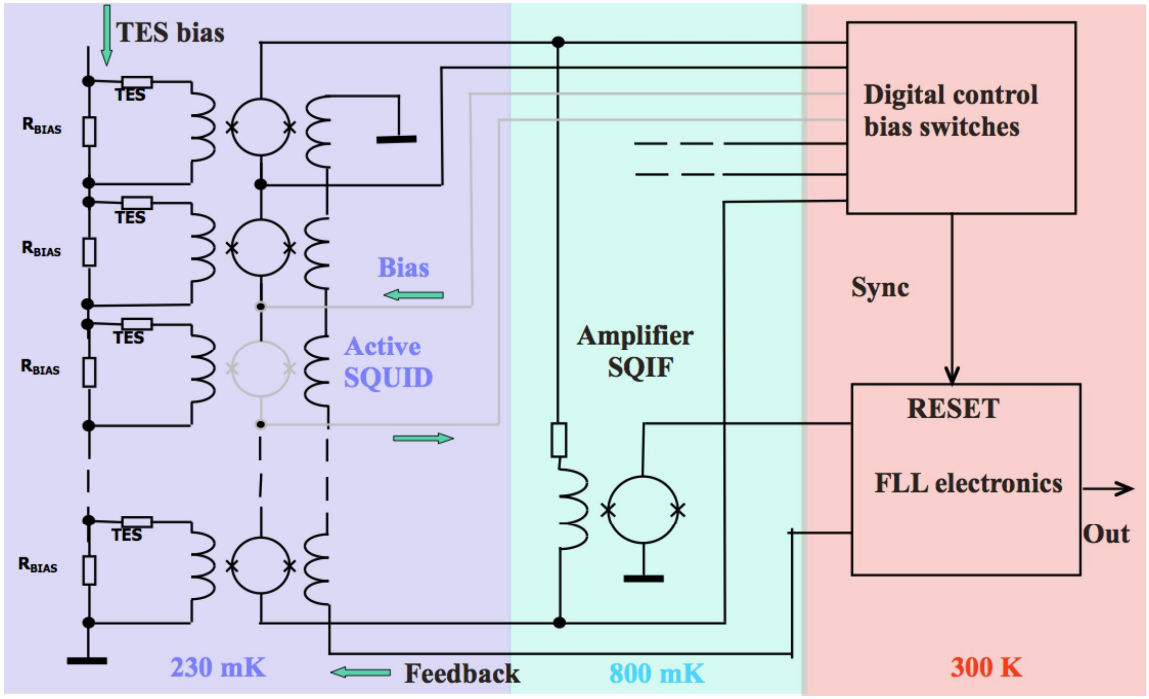

Figure 23: Schematic of the readout electronics of LABOCA-2

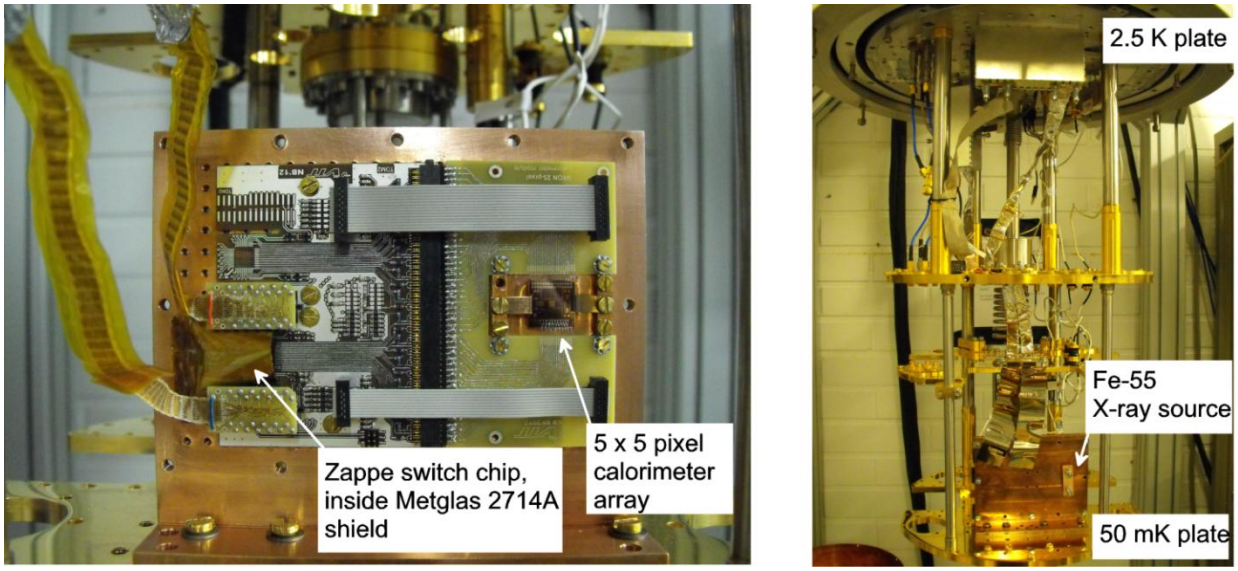

Figure 24. Time-domain 8-pixel multiplexing demo setup. Left: the opened experimental box with the calorimeter array and the superconducting switch chip inside a magnetic shield. For a closeup of the switch chip see Figure 28. Right: the experimental box installed in dilution refrigerator.

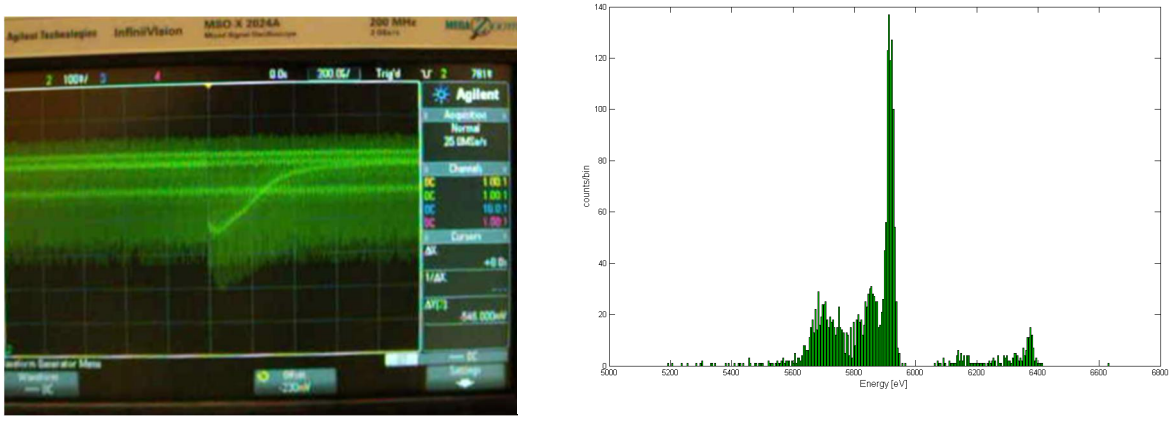

Figure 25. Left: screen capture of the real-time signal traces when the TDM circuit is operated in 4-pixel mode and one pixel captures an X-ray event. The 'hair' in picture are glitches at the time slot edges, which are decimated away from the histogrammed data. Right: an energy histogram showing the 5.9 keV α-complex of the 55-Fe source.

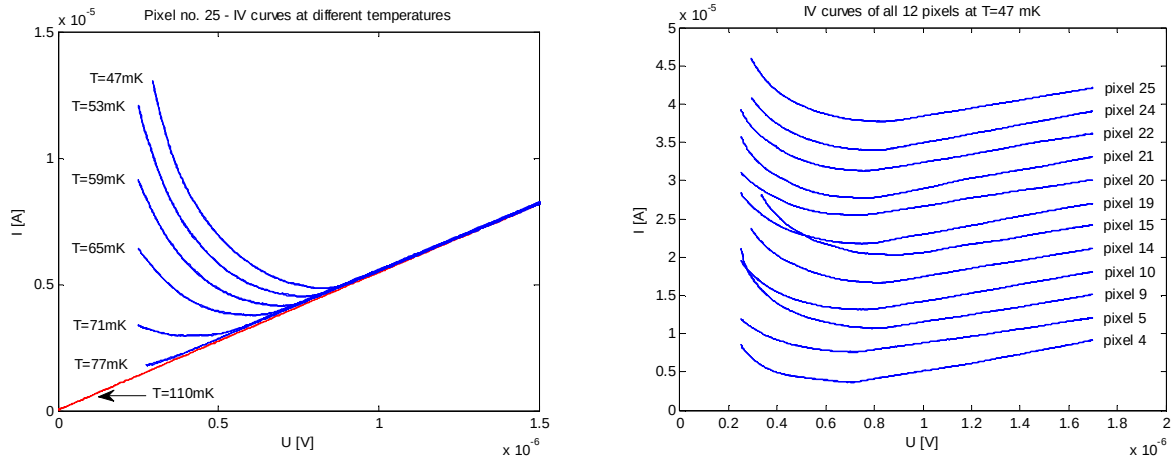

Figure 26. 'BESSY' 5 x 5 calorimeter array characteristics measured with the superconductive switch chip. Left: IV characteristics of one pixel at various temperatures. Right: characteristics of twelve pixels, measured in single cooldown. Characteristics are shifted by 3 μA steps for better clarity.

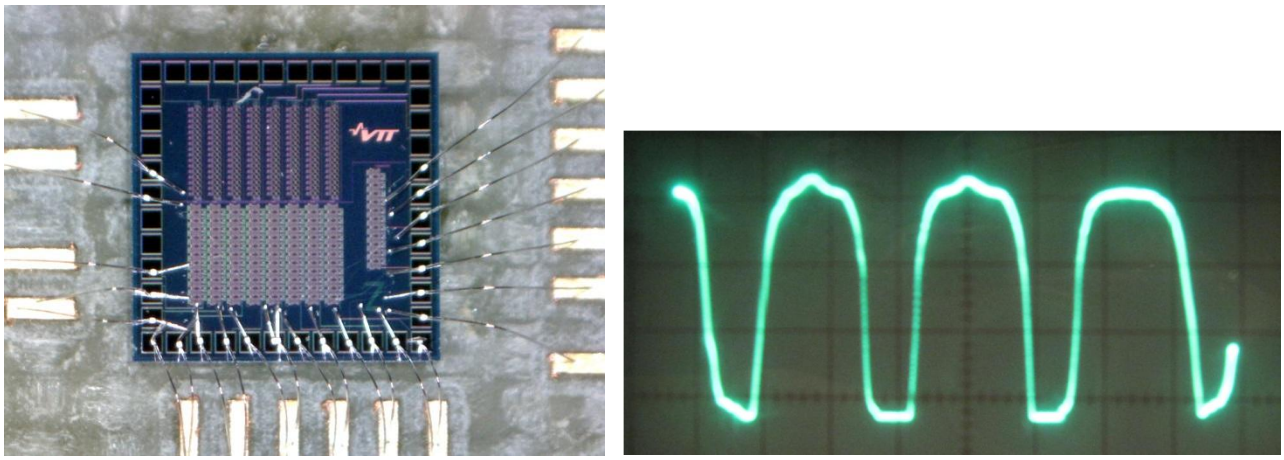

Figure 27. Left: microphotograph of the VTT-fabricated superconductive switch chip, installed in a test setup. Right: flux response of the 48-series Zappe interferometer array.

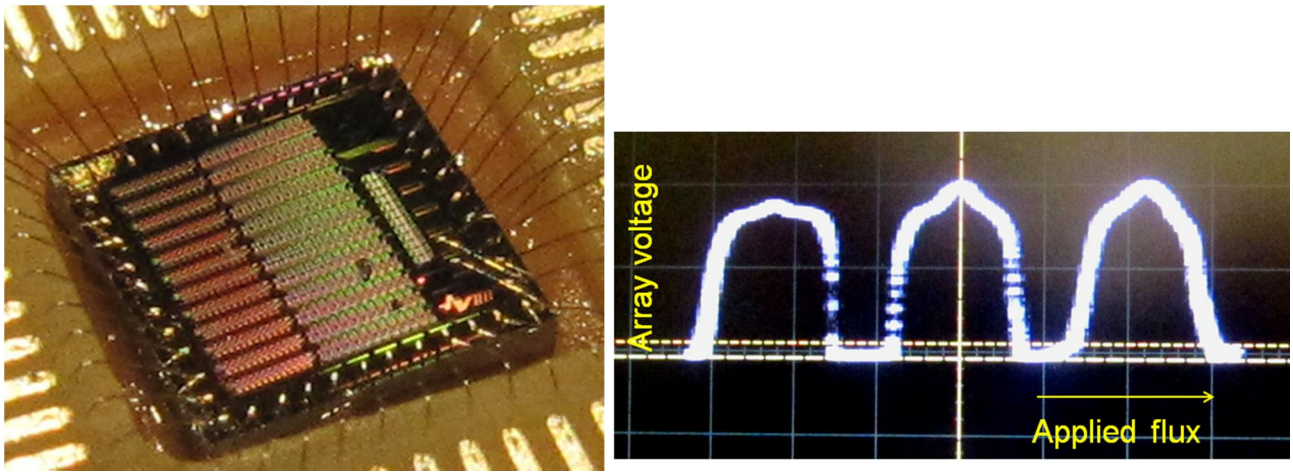

Figure 28. Left: Microphotograph of the IPHT-fabricated superconductive switch chip, installed in the 8-channel TDM multiplexing demontrator. Right: flux response of the 48-series Zappe interferometer array.

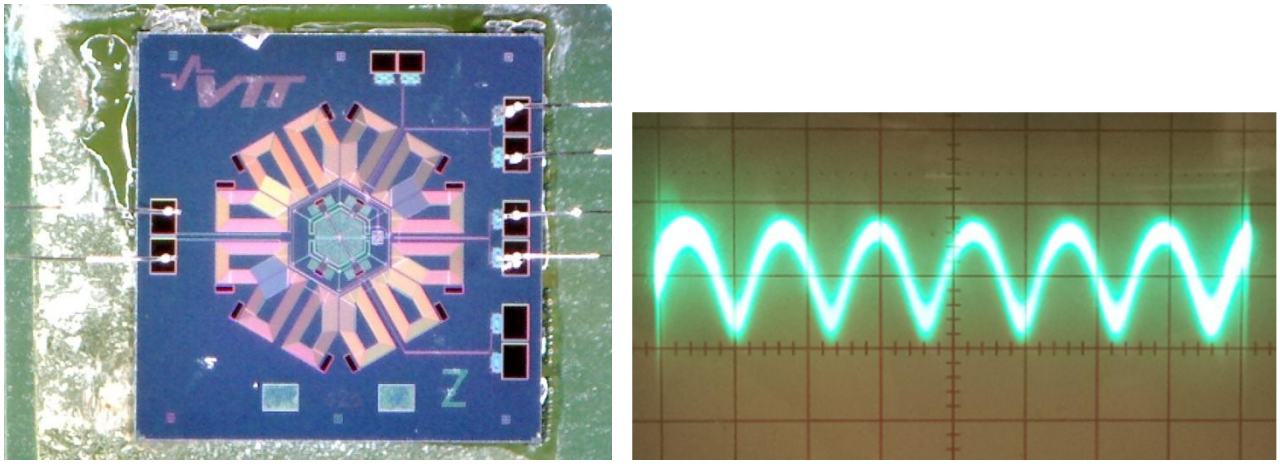

Figure 29. Left: Microphotograph of the SQUID amplifier intended for the 'high-Z summing point' experiment. Right: flux response shows 0.8 μA/Φ_0 periodicity.

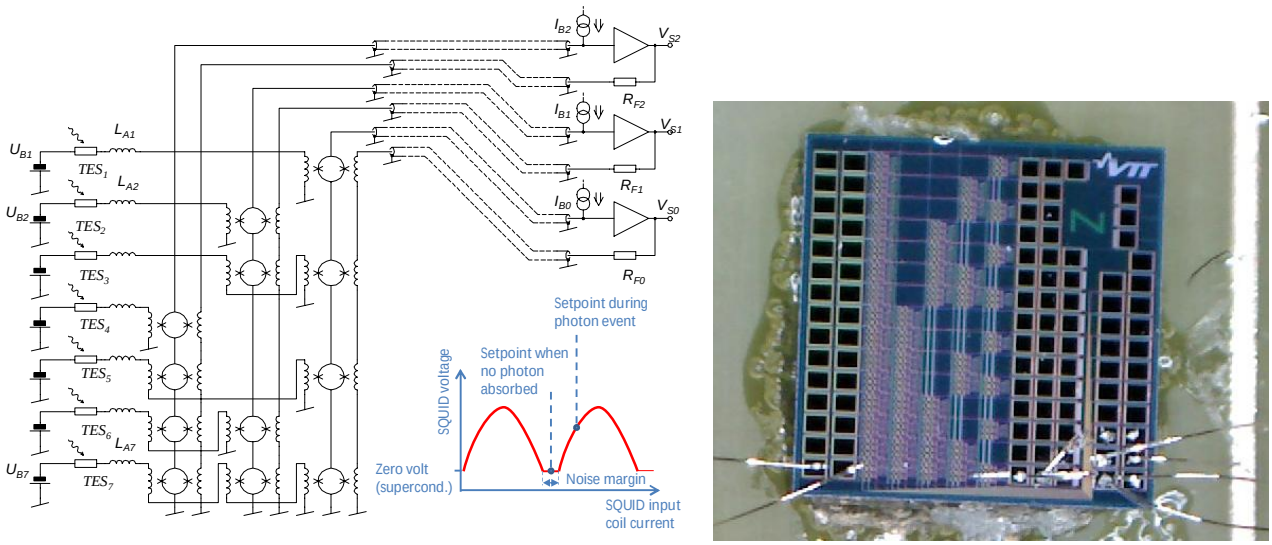

Figure 30. Left: SQUELCH circuit, principle of operation. Right: microphotograph of the 16-channel SQUELCH chip, cascadeable to 32 channels.

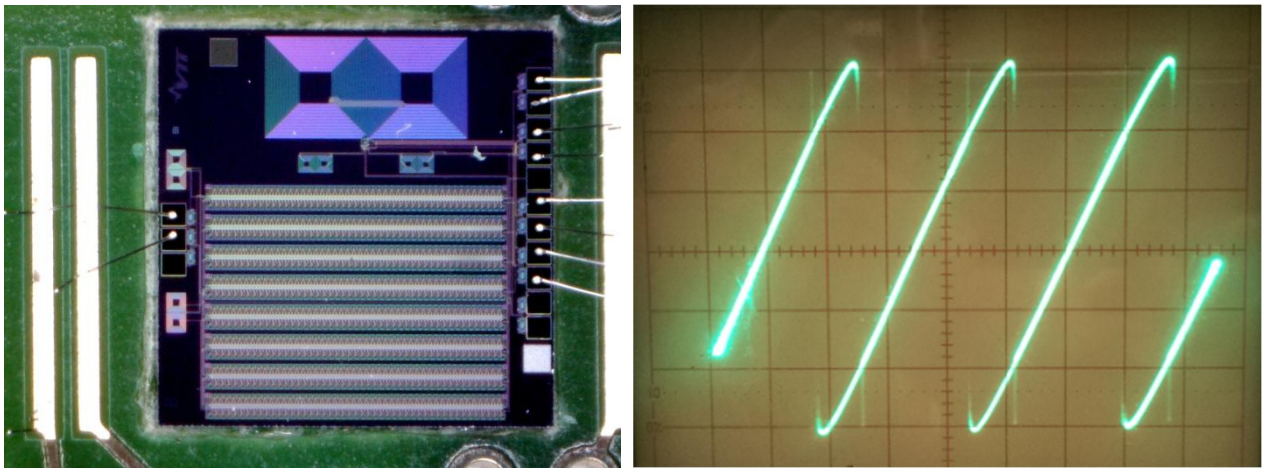

Figure 31. Left: Microphotograph of the version of a 4x184 SQUID array equipped with integral Lin-screening transformers. Right: flux response of a 4x184 array when operated in locally linearized mode.

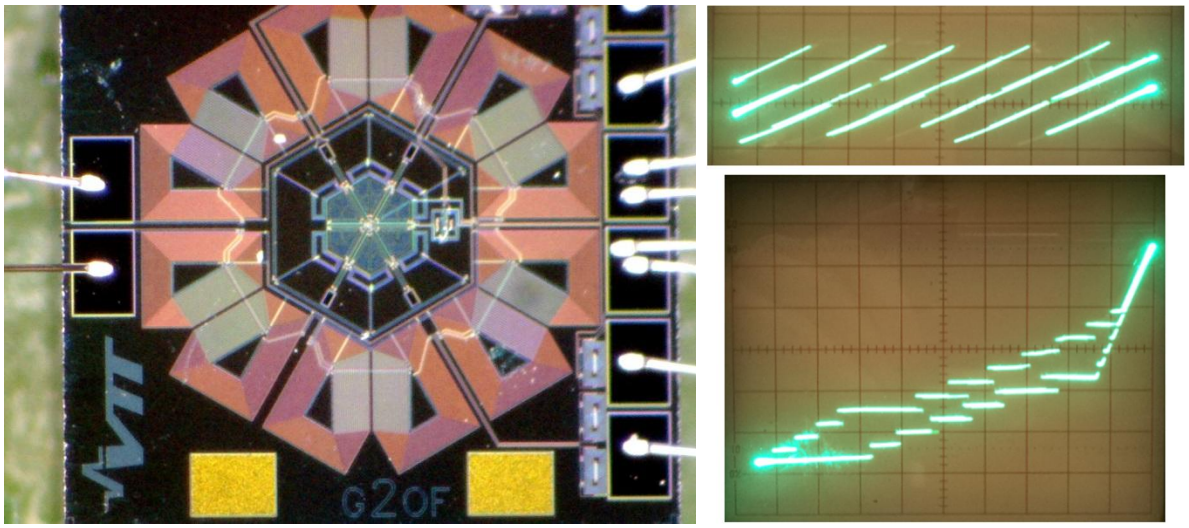

Figure 32. Left: microphotograph of the locally linearizable multiloop SQUID. Right top: flux response when the SQUID is operated at local loop gain of 5.5 . Right bottom: IV-characteristics of the SQUID show plateaus when local feedback is active. Horizontal axis is bias voltage and vertical axis is SQUID current, showing a part of the the superconductive branch.

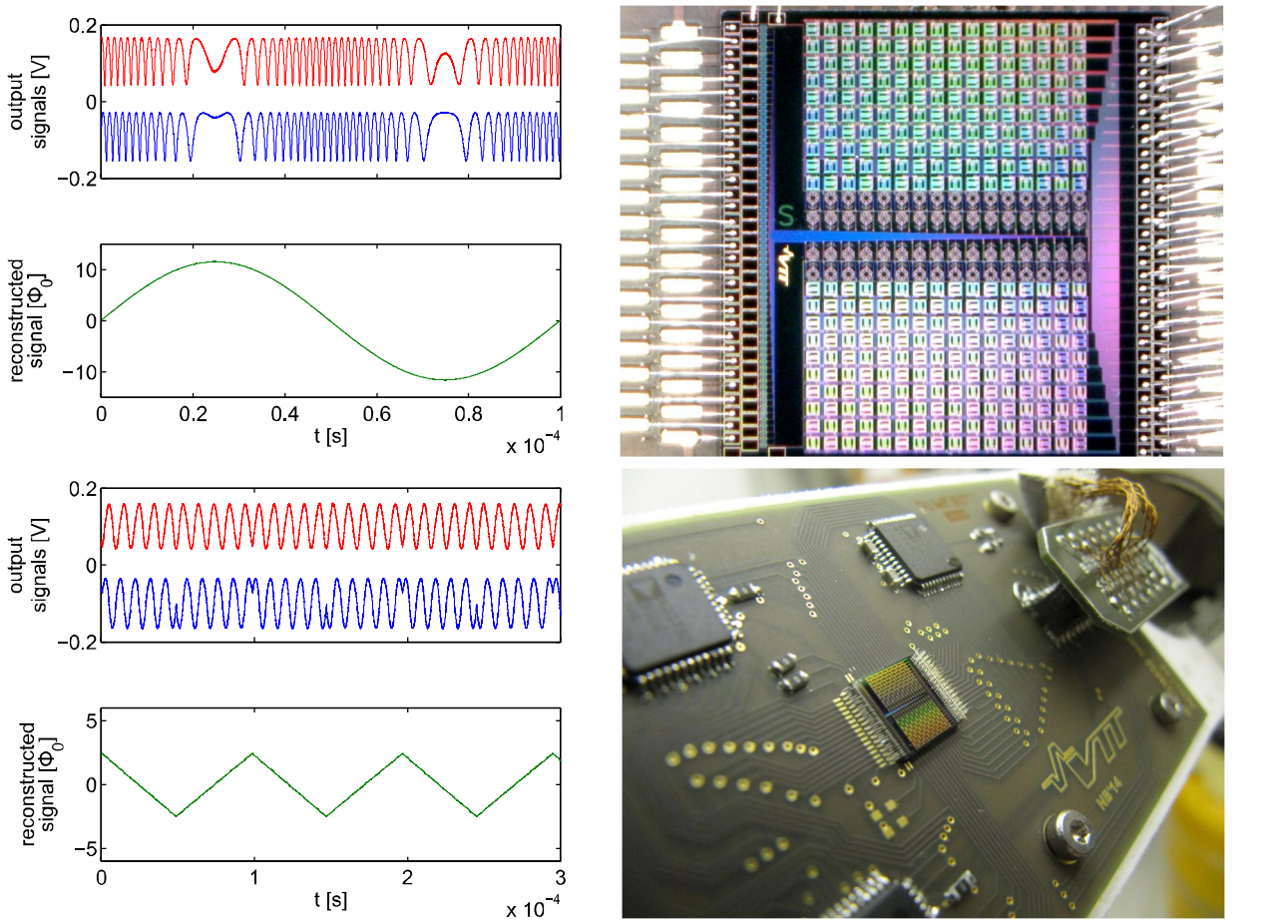

Figure 33. Left: results from sin/cos flux counting experiment. Top half shows the sin(ϕ) and cos(ϕ) quadrant SQUID signals, and the reconstructed excitation, when 10 kHz sinusoid with 20 Φ_0 p-p amplitude was applied. Bottom half shows the signals when triangle wave with 5 Φ_0 p-p amplitude has been used as excitation. Right: sin/cos flux counting approach has been implemented in a 32-channel flux-summing Code Domain Multiplexer chip, to solve the dynamic range problem without increasing dissipation. Experiments are underway and still inconclusive.

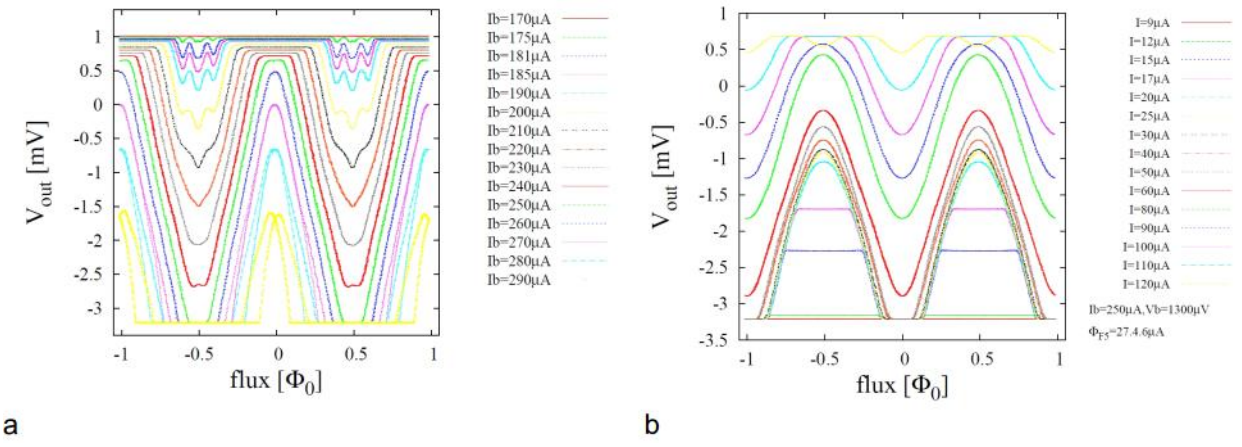

Figure 34 a). Voltage-to-flux characteristics of the F5 SQUID array as a function of SQUID bias current. The F5 SQUID operates at 20mK in a two-stage configuration with G1 SQUID array superconducting. B). Voltage-to-flux characteristics of the two-stage SQUIDs (F5 and G1) configuration operating at 20mK. The input coil of the G1 SQUID was open.

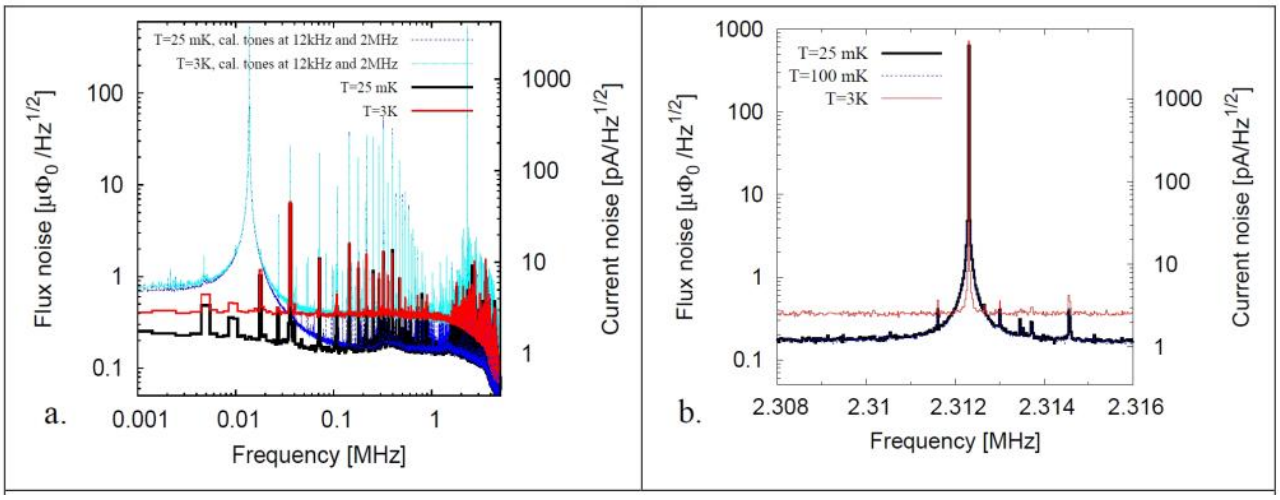

Figure 35 a) Flux and current noise spectra density for the two-stage SQUIDs F5+G1 configuration measured at at 3K and 20mK. B). Zoom-in at about 2 MHz. The spikes in the noise spectra and the roll-off at about 3MHz are due to a combination of the room temperature electronics and the data acquisition system.

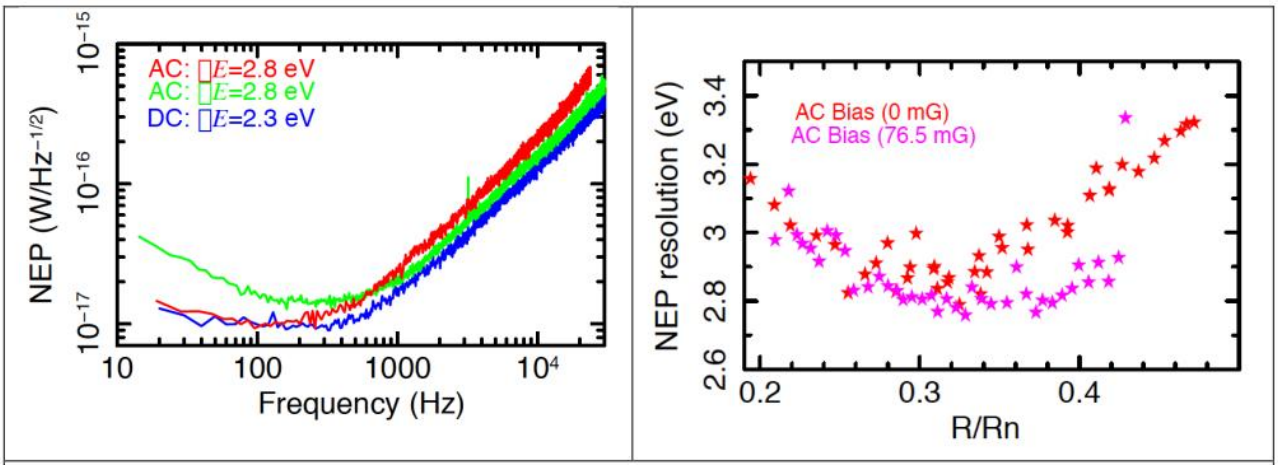

Figure 36: Measured noise equivalent power (NEP) vs frequency (left) and integrated NEP vs normalized setpoint resistance (right) for a microcalorimeter pixel which is transformer coupled to the LC resonator and SQUID with a turns ratio of 5, to properly match the impedance levels. The left-hand plot shows the measured NEPs for different settings of the anti-alias filter, and under AC and DC bias. Depending on the settings, either the NEP at the high or the low frequency side of the spectrum overlap. Further work on the electronics is needed to solve this issue. The plot on the right hand side shows that the integrated NEP is better than 3 eV over a range of bias points, and depends on the applied magnetic field.

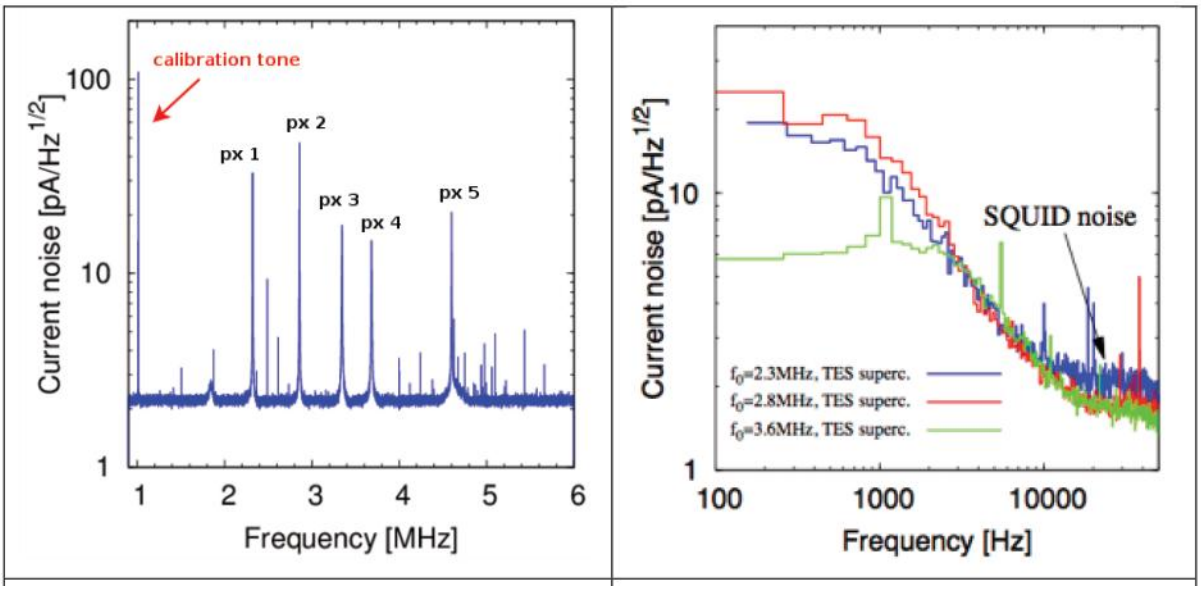

Figure 37: (left) Measurement of the current noise spectral density as function of frequency with the TESes in the superconducting state. The pixel numbers are labeled. At the resonances the Johnson noise of the resonators is dominant, while in between the resonances the equivalent input current noise spectral density of the SQUID is observed directly (~2.2 pA/ √Hz). The calibration tone has been used to calibrate the transfer function of the amplifier chain.

Figure 38: (right) 8: Current noise spectral density of 3 resonators after demodulation with the digital baseband feedback electronics. The low SQUID noise level as observed in Figure 7 remains conserved after demodulation. The higher noise level below 1 KHz is expected from the small stray resistances in the high-Q LC filters.

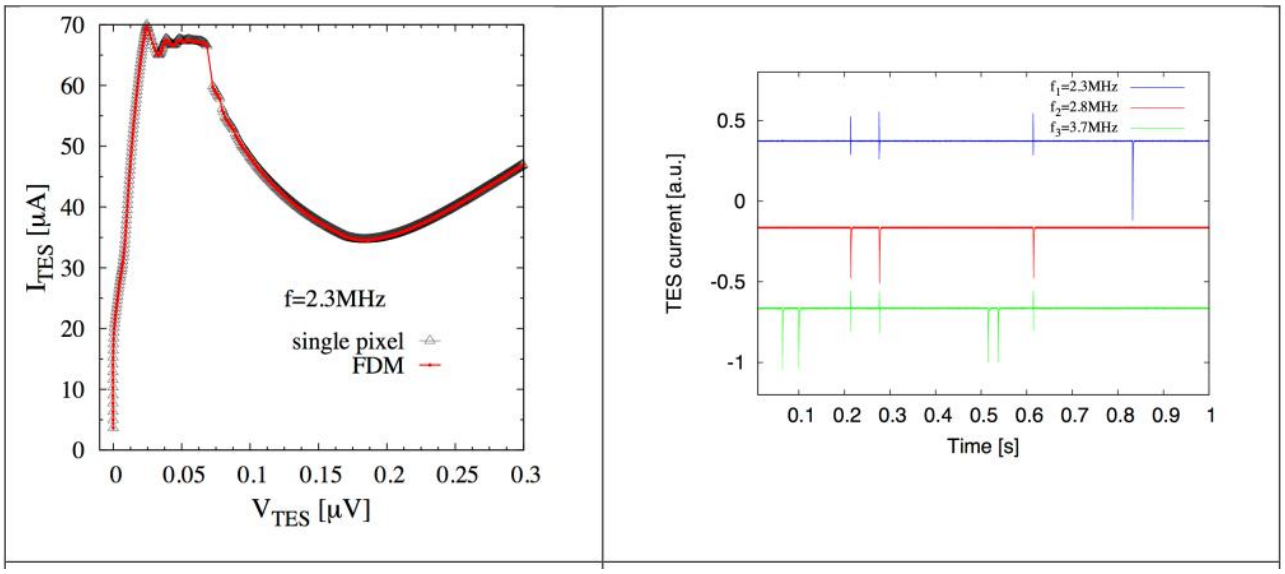

Figure 39: (left) Comparison of an IV curve of a microcalorimeter measured with 3 other pixels on (FDM mode, red) and with the 3 other pixels off. As the curves overlap, this result shows that multiple pixels can be switched on, without observing influence on the bias power of a single pixel.

Figure 40: (right) Time domain plot of 1 second of bias current data taken from 3 pixels simultaneously, at 3 different frequencies. The single sided signals are photon responses, and the double sided signals are cross talk events. The demonstration is qualitative only.

Text

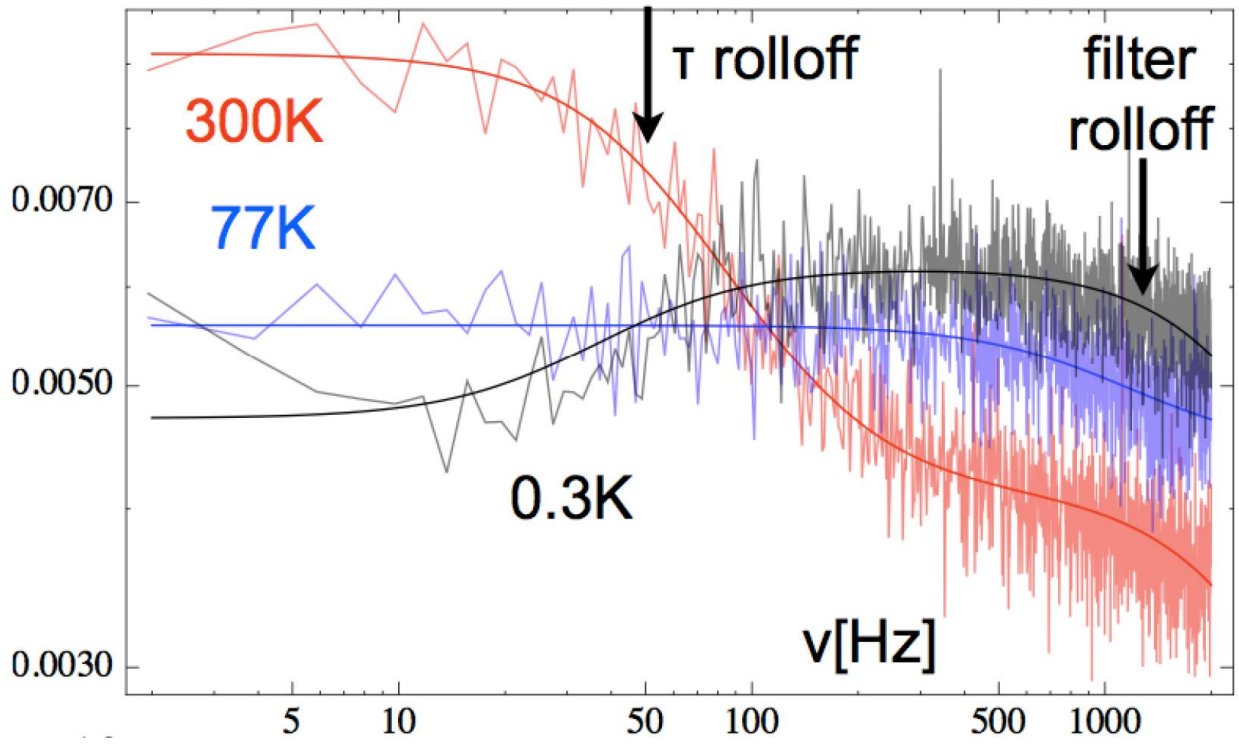

Figure 41: Evidence of background photon noise at 870μm wavelength. At high frequencies the rolloff is due to the ADC. The time constant derived from the 300K photon noise is 2.8ms, close to that measured directly. The ratio of the noise at low frequencies is near to that expected, as is the ratio of the Johnson noise at high frequencies.

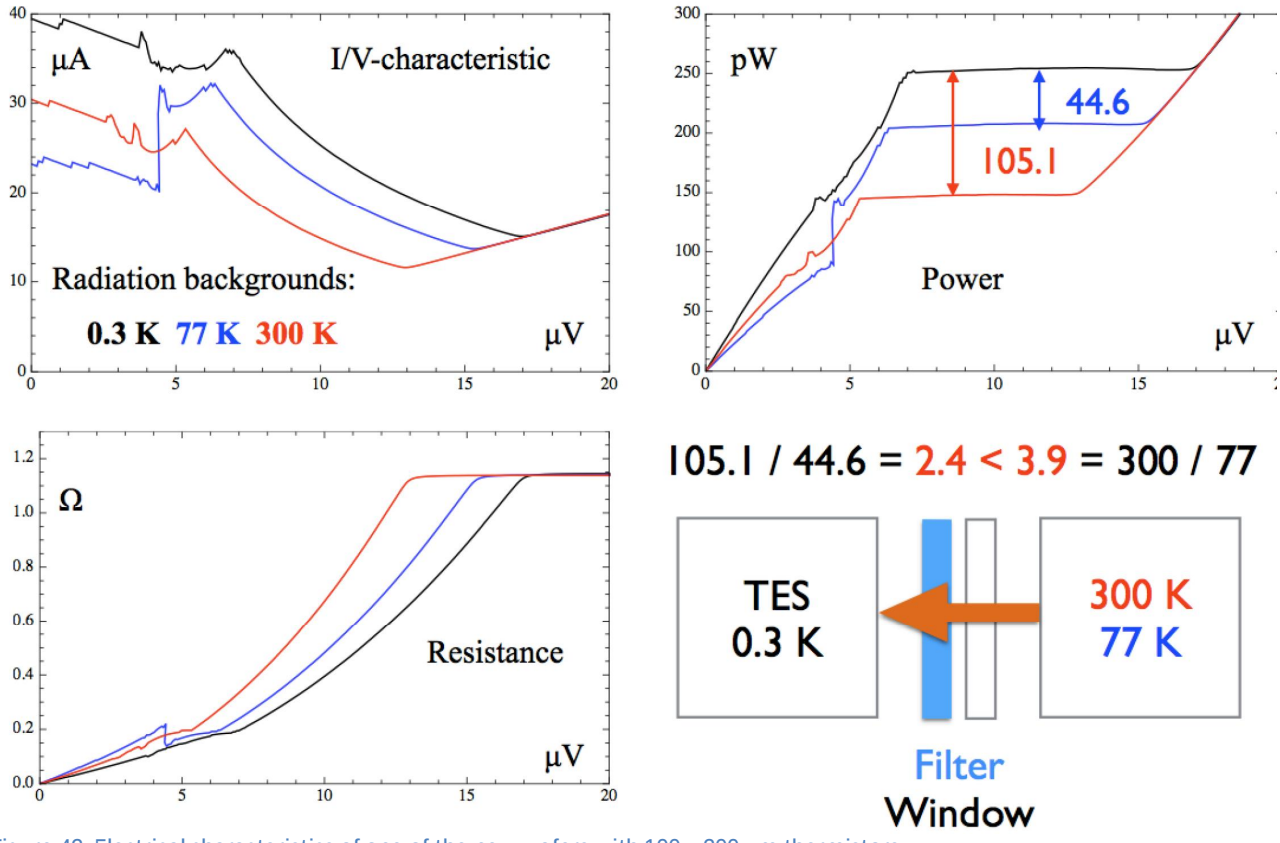

Figure 42: Electrical characteristics of one of the new wafers with 100 x 200 μm thermistors

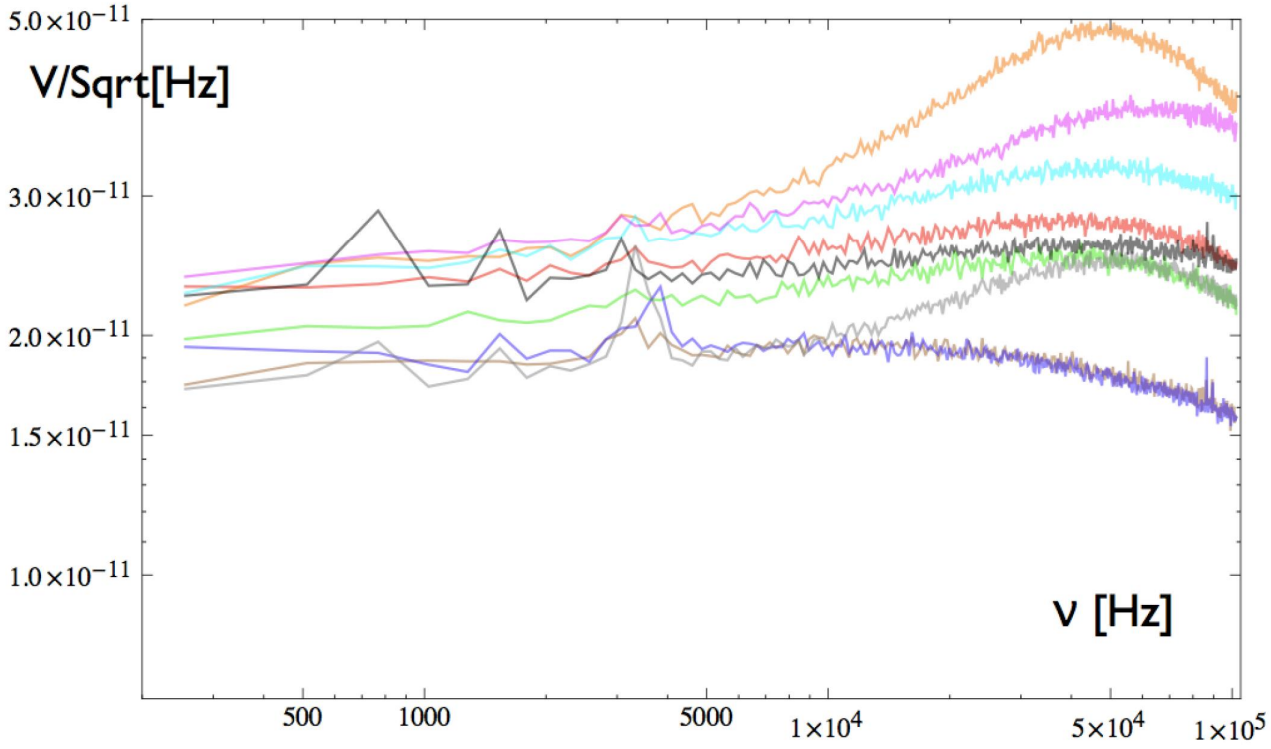

Figure 43: Excess high frequency noise of the TES on the wafer

Bias is 1.9 V , about 0.2 V below the normal transition. Pulse tube is on.

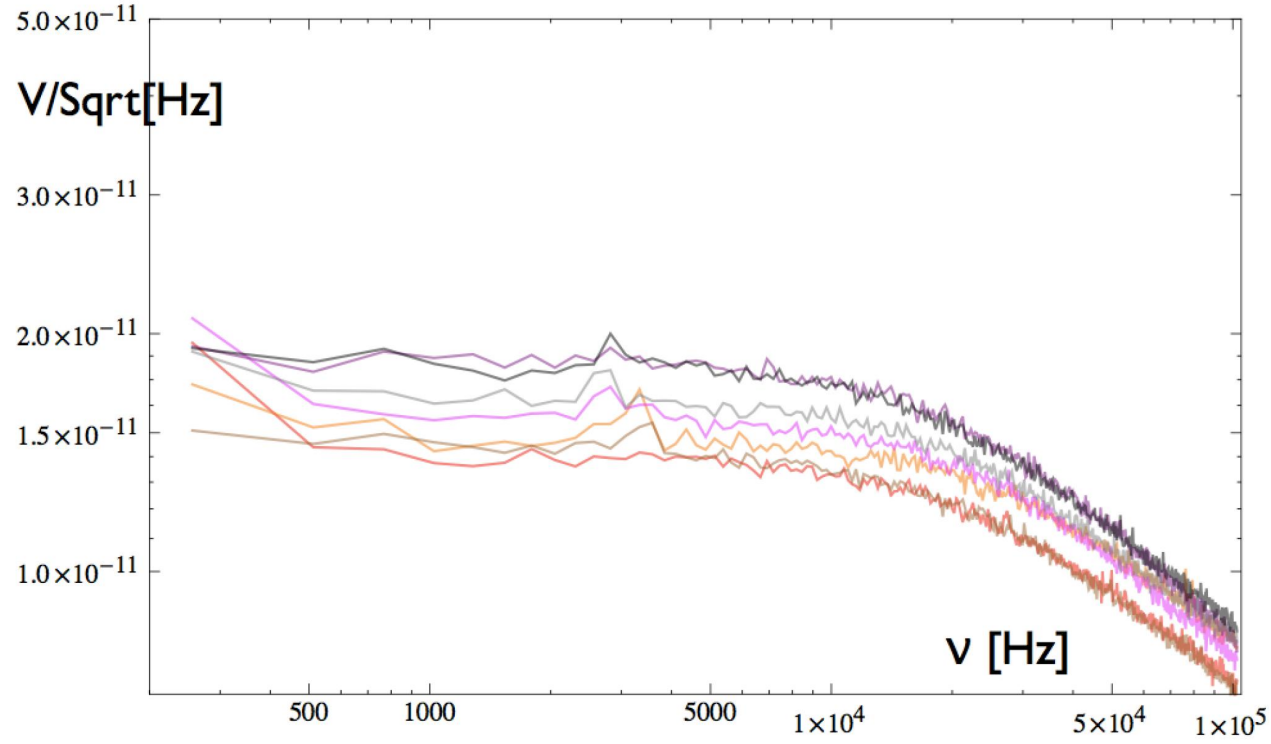

Figure 44: High frequency noise for all seven TES on the test chip. Bias is 0.2V below normal transition. Pulse tube is on.

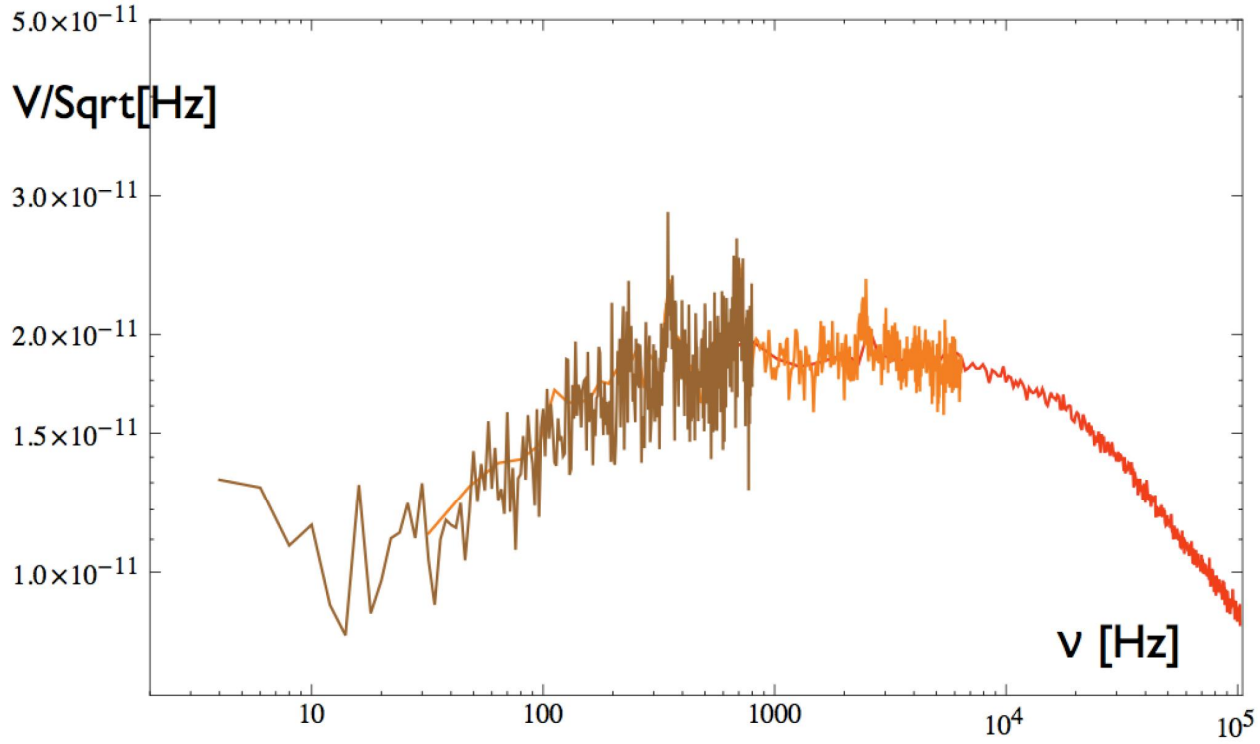

Figure 45: Noise of that TES on the test chip that is most similar to the TES on the wafer. Pulse tube is off.

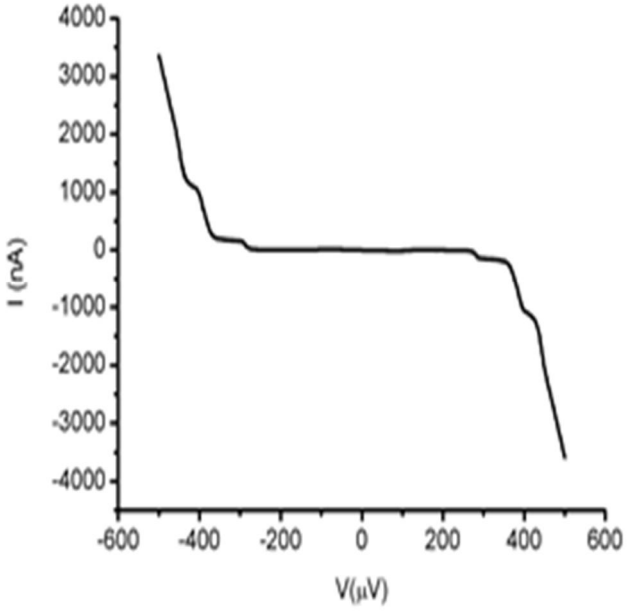

Figure 46: *IV curve of a STJ when a magnetic field is applied to suppress the Supercurrent*

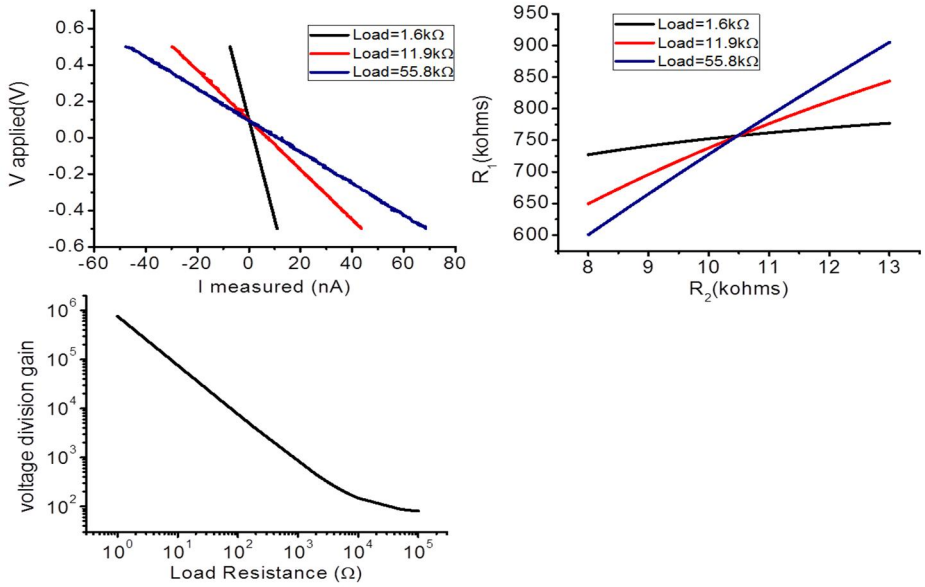

Figure 47: *Calibration of the voltage divider gain.*

Top left, the voltage applied at the input of the voltage divider is plotted versus the measured current for 3 different resistance load. Top right, graphical determination of the two equivalent resistors of the voltage divider. Bottom left, voltage divider gain versus the load resistance deduced from the resistors value.

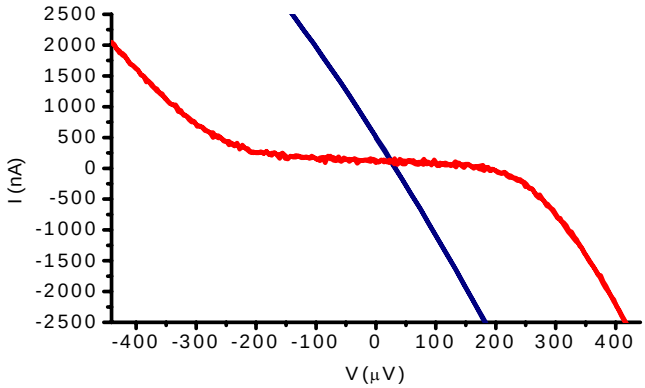

Figure 48: *IV curves measured with the cryogenic amplifier*

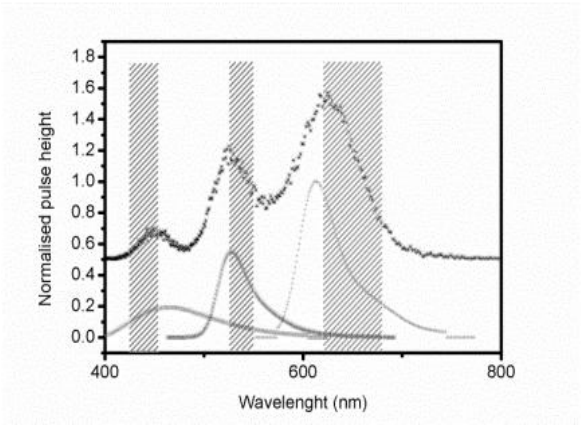

Figure 49: *Measured spectrum obtained using a triple filter set (black dot).*

The data have been shifted along the vertical axis. Emission spectra as published by the manufacturer are also shown.

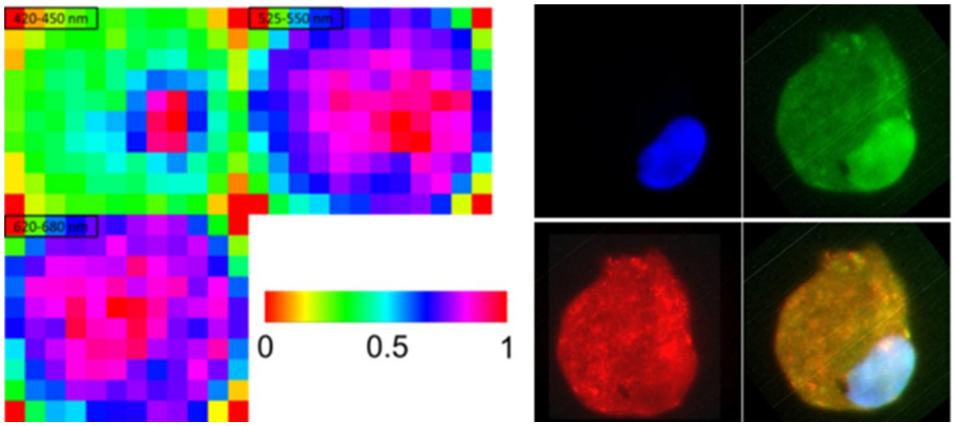

Figure 50: (a) *(Left) Multispectral images of a human fibroblast cell acquired with the S-CAM. Each image considers only photons with wavelength in the indicated band*

(b) (Right) CCD images of the same cell obtain using 3 different filters optimised for each staining dyes. The last image is an overlay of the three others).

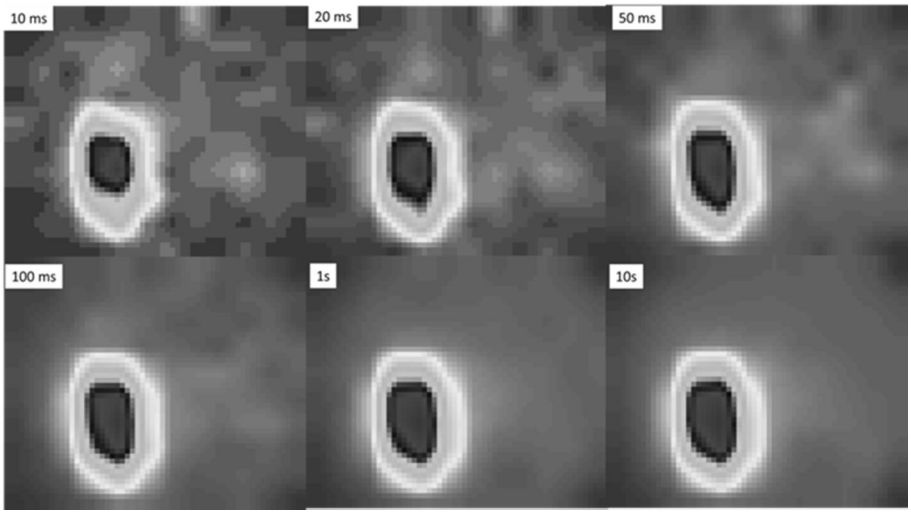

Figure 51: Human fibroblast cell after DAPI staining imaged with filter set A, for different time of integration (from 10 ms to 10s). Already after few milliseconds the nucleus is clearly observed. In this image the number of pixels have been artificially increased from 12x10 to 120x100 using the "scale" procedure of the public domain software imageJ